PHYSICAL REVIEW E **84**, 035202(R) (2011)

Whispering gallery modes formed by partial barriers in ultrasmall deformed microdisks

Jeong-Bo Shim,[1] Jan Wiersig,[1] and Hui Cao[2]
[1]*Institut für Theoretische Physik, Otto-von-Guericke-Universität Magdeburg, D-39016 Magdeburg, Germany*
[2]*Department of Applied Physics, Yale University, New Haven, Connecticut 06520-8482, USA*
(Received 21 December 2010; revised manuscript received 13 July 2011; published 19 September 2011)

Unexpected formation of regular high-Q whispering gallery modes in a deformed microdisk where the radius is of the order of the vacuum wavelength is explained in terms of partial barriers in phase space. Using a semiclassical approach to determine the action flux of the partial barriers, we successfully predict spectral ranges in which the high-Q modes can exist. Our analysis enables optimization of emission directionality and the Q factor of deformed ultrasmall microcavities.

DOI: 10.1103/PhysRevE.84.035202 PACS number(s): 05.45.Mt, 03.65.Sq, 42.55.Sa, 42.60.Da

For the past few decades, microcavities with whispering gallery modes (WGMs) have become indispensable elements in nano-optics [1], mainly because they can confine light for a long period of time and allow for extremely high quality-factor (Q-factor) modes with micrometer-scaled structures [2]. Using this property, several unique devices are developed from optical switches to optical sensors, and also various unprecedented optical phenomena such as optomechanical vibration [3] and strong interaction of atoms and photons [4] are realized.

Furthermore, the application domain of microcavities with WGMs is broadened through the deformation which enables directional light emission from WGMs by breaking the rotational symmetry [5]. In the process of deformation, the Q factor is reduced, but a considerable portion of the modes still has high Q factors. The deformed microcavities have been experimentally realized with several different cross-sectional shapes and various materials [6–10]. Also, they become important models in the field of quantum chaos [11,12] for the study of ray-wave correspondence in open systems [13–17].

Nonetheless, it is not easy to understand and predict the spectrum and emission directionality because the internal ray dynamics is chaotic due to the broken rotational symmetry. Therefore, many studies have concentrated on the properties of the spectrum and the role of the chaotic dynamics to generate directional light emission from high-Q WGMs. As a result, the studies reached a common conclusion, at least in the emission directionality, that the overall dynamical flow following unstable manifolds in the phase space determines the emission directionality [15,16].

Currently, experiments in micro-optics pursue fabrication of smaller cavities to improve the single-mode availability for laser operation or sensitivity of optical sensors [10]. Accordingly, deformed microcavities are realized in such a ultrasmall regime where the vacuum wavelength λ is of the order of the length scale of the cavity size R, i.e., $R/\lambda \sim 1$ [8,9]. In this regime, high-Q WGMs still exist, but the emission from them is not as directional as from larger cavities, and the ray dynamical prediction of emission directionality is not valid anymore, because the resolutions of the modes are not enough to follow the fine structures in chaotic phase space [17,18]. So far, only the possibility of accidental coupling with low-Q modes is known to lead to directional emission [9].

However, such a limit of the resolution can induce a stronger suppression of chaotic mixing and diffusion than dynamical localization in cavities with a surface roughness in a higher spectral regime ($R \gg \lambda$) [19]. Hence, a better predictability of optical properties can be expected. In this Rapid Communication, the theoretical analysis on the high-Q WGMs in ultrasmall microcavities is performed. Applying a semiclassical quantization scheme with consideration of openness, the mechanism which suppresses the directional emission and constructs the high-Q WGMs is clarified. Furthermore, the spectral criteria for high-Q WGMs are derived and confirmed by comparison with numerical data. Though our results are relevant for all deformed ultrasmall microcavities (microspheres, etc.), we focus in this Rapid Communication on the microdisk of Limaçon shape, the boundary of which is given by $r(\phi) = R(1 + \varepsilon \cos \phi)$ in polar coordinates. This microcavity shows unidirectional light emission and high Q factors for sufficiently large R/λ [16] [Fig. 1(a)], the shape of which has been experimentally realized [7–9]. In this Rapid Communication, the deformation parameter ε is set equal to 0.43 and the refractive index n is set as 3. To analyze the ray dynamics in this cavity, the Poincaré surface of section (PSOS) can be obtained by recording the position of the ray on the boundary along the perimeter S in units of R and the sine value of the reflection angle $\sin \chi$ as a corresponding canonical momentum at every bounce [see Fig. 1(a)]. As Fig. 1(b) shows, the ray dynamics is strongly chaotic in most of the PSOS. The spectrum of the model system is numerically calculated using a normalized frequency $R\omega/c = kR$ and the boundary element method [20]. Figure 2(a) presents the spectral data in $2 \leqslant \mathrm{Re}(kR) \leqslant 25$ for transverse magnetic (TM) polarizations. The polarization of modes does not affect the physical essence of this work. The noteworthy feature of this spectrum is that there are convex curved mode series with local maxima of the Q factor which are denoted by colored (black) symbols in Fig. 2(a). More intriguingly, these mode series show an inverse tendency in the property of unidirectional emission [Fig. 2(b)]. To quantify the directionality of the emission, we introduce a measure of unidirectionality $U = \int_0^{2\pi} \cos\theta f(\theta) d\theta$, where $f(\theta)$ is the normalized far-field distribution of the given mode [9].

A clue to reveal the physics behind this observation can be found in the individual mode distribution. Figures 3(a)–3(c) are the spatial distributions of the modes, which are located in the spectrum around the top of each curved mode series. A striking feature is the existence of well-defined mode numbers in the spatial mode distributions. As Figs. 3(a)–3(c)

RAPID COMMUNICATIONS

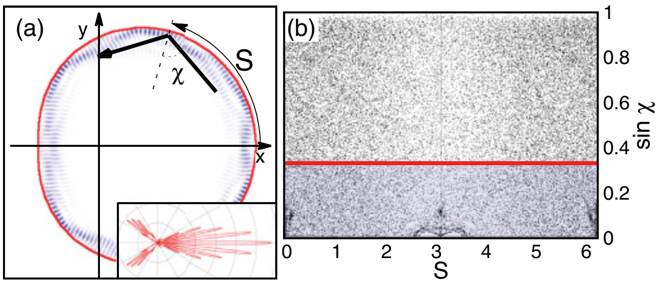

FIG. 1. (Color online) (a) Optical mode in a normal-sized Limaçon cavity with $\varepsilon = 0.43$. The superimposed coordinate system is implemented for the PSOS. Inset: Far-field intensity distribution of the mode. It shows a strong unidirectional emission to the right-hand side. (b) PSOS for the same system. Strong chaos is generated above the critical line $\sin\chi = 1/n$, denoted by the horizontal line. The area under the line is the leaky region, where the total internal reflection condition is not satisfied.

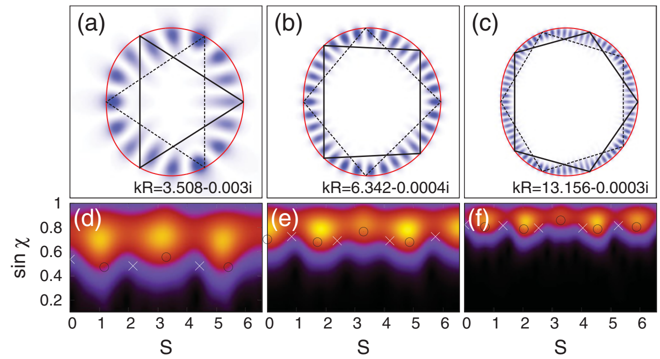

FIG. 3. (Color online) (a)–(c) Spatial pattern of high-Q WGMs which are confined by partial barriers of periodic orbits. (a) Period-3, (b) 4, (c) 5. (d)–(f) Husimi distributions corresponding to (a)–(c), respectively. Pairs of Birkhoff periodic orbits are denoted by $\odot$ (dashed line) and $\times$ (solid line).

demonstrate, all of the modes have very regular distributions in the configurational space, i.e., one node along the radial direction and $2m$ along the azimuthal direction, such as (a) $m = 8$, (b) $m = 16$, and (c) $m = 35$ in Fig. 3. As can be seen from the invariant torus quantization, such a feature is typical for an integrable or near-integrable system. However, considering the strong chaos and tiny regular region on the top side of the phase space in Fig. 1(b), these features are counterintuitive.

When we superimpose a pair of periodic orbits with p-periods ($p = 3$–6) which are supported by Poincare-Birkhoff's theorem [21], another interesting feature is revealed, i.e., the configurational distributions of the modes fit well to the area between the boundary and the inner side of the pair of the periodic orbits, as shown in Figs. 3(a)–3(c). This observation is also confirmed by the Husimi distributions [22] in the PSOS. Figures 3(d)–3(f) show that each Husimi distribution has the average value of $\sin\chi$ well preserved from the angular momentum of the cylindrical microcavity mode with the same

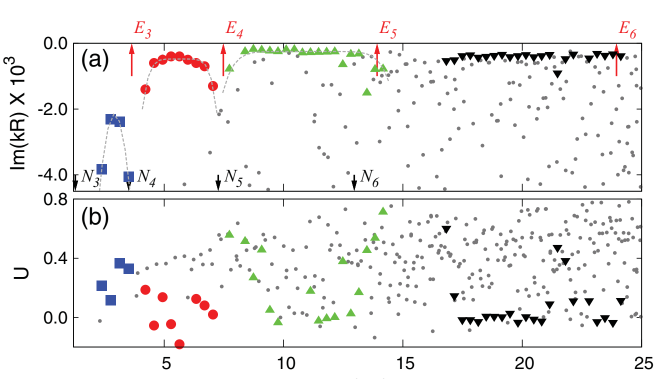

FIG. 2. (Color online) (a) Spectrum of normalized complex frequencies kR. Each symbol corresponds to a mode. The local maximum of $Q = -\mathrm{Re}(kR)/2\,\mathrm{Im}(kR)$ is reached by a convex curve plotted by colored symbols. The symbols mark the geometry of the confining partial barrier. ■ (blue): period-3; ● (red): 4; ▲ (green): 5; ▼ (black): 6. (b) Corresponding measure of unidirectionality. The opposite tendency to Q factors is visible.

mode numbers, and the lower tail of it is bounded by the fixed points of periodic orbits. This implies that chaotic diffusion in the deformation process is somehow suppressed, supposedly by the periodic orbits. Also we can see the distribution is localized above the $\odot$ points [23].

To explain these findings, we first focus on the remnants of the broken dynamical invariant structures in phase space. In the case of a circular cavity, all periodic orbits with the same period lie on an impenetrable invariant line in the PSOS. However, when the nonlinear coupling in the internal ray dynamics is induced by the boundary deformation, the line disappears and only the Birkhoff periodic orbits remain. In this case, we can define a partial barrier with a line which fills the gaps between the periodic orbits and the corresponding action transport which measures the amount of trajectories passing through it [24]. For this purpose, initial conditions are chosen on the lines placed on the left-hand part of the PSOS for the periodic orbits (denoted by red dashed-dotted lines in Fig. 4), and iterate them backward and forward until they reach the central gaps of the fixed points, which allows us to obtain a curve consisting of the initial lines and the image of them (black lines). With the resulting curve the partial barrier of a periodic orbit can be defined and the PSOS is divided into an upper and a lower part. At the central gap of each periodic orbit, there are two areas enclosed by the backward (green dotted) and forward images (black solid) of the initial lines (W_p's in Fig. 4). With these areas the characteristic action transport of each periodic orbit, i.e., the amount of trajectories passing upward and downward through the partial barrier, is defined. These areas are called the *turnstile* [24].

Applying the semiclassical quantization to entities of the partial barrier, we can then set a hypothesis as the following conceptual sketch: As the wave number of a corresponding mode is increased, the resolution in phase space gets accordingly higher. When the resolution reaches the area above the partial barrier of a periodic orbit chain (marked by A_p in Fig. 4), then one mode can be formed in this area. We call the corresponding value of $\mathrm{Re}(kR)$ the *entering point*. At this point, the turnstile area ($W_p \ll A_p$) is still far below the resolution limit, therefore the partial barrier is able to confine the mode efficiently. However, when the wave number

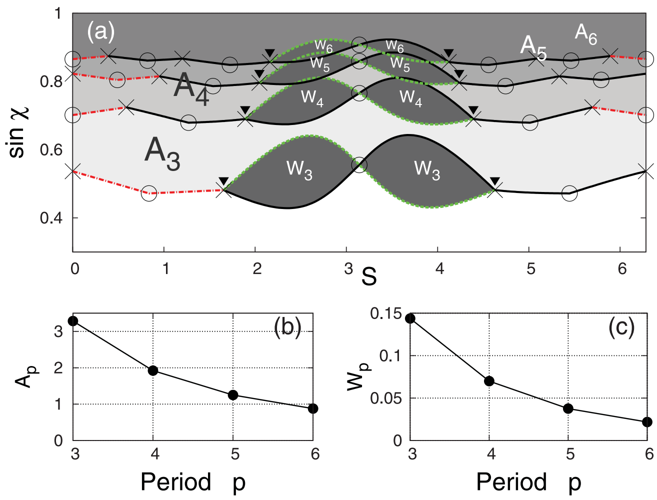

FIG. 4. (Color online) (a) Turnstiles of periodic orbits in PSOS: The areas W_p's at central gaps (between ▼-marked fixed points) are enclosed by the forward (black solid curves) and backward image (green dotted curves) of initial lines (red dashed-dotted lines) connecting two consecutive fixed points (×) through a fixed point (⊙) from the other periodic orbit of the Birkhoff pair. (b) Areas A_p's above the partial barriers. (c) Turnstile area (action flux) W_p.

is increased high enough to resolve the turnstile, the mode can escape from the confinement and all the corresponding features of a wave function disappear accordingly. We name the corresponding value of $\mathrm{Re}(kR)$ the *escaping point*. Based on this hypothesis, more detailed and precise conditions are deduced to allow for a quantitative comparison with the spectral data. First, a condition for the entering point is derived. On account of the regular formation of the modes, we use the analogy with WGMs in circular cavities and modify their semiclassical quantization condition in terms of PSOS areas. In a circular cavity, the governing wave equation can be separated into radial and azimuthal degrees of freedom. The radial motion can be described by a one-dimensional wave equation with total energy $E_{\mathrm{tot}} = 1$ and effective potential $V_{\mathrm{eff}}(r) = (r_0/r)^2 + [1 - \overline{n}^2(r)]/n^2$, where $\overline{n}(r) = n(r \leqslant R), 1(r > R)$, and $r_0 = R \sin\chi$ [Fig. 5(a)]. The semiclassical quantization condition is applied to the oscillatory radial motion in this effective potential to obtain a ground state along the radial direction. Then the following inequality is formulated for the minimum wavelength that allows a mode to lie in the area above a partial barrier in the PSOS:

$$\mathrm{Re}(kR) > \frac{1}{n}\frac{\pi/4 + \alpha_p}{\sqrt{1 - X_p^2} - X_p \cos^{-1}, X_p}, \tag{1}$$

where α_p is a phase sliding resulting from the Fresnel factor, $X_p = 1 - A_p/S_{\mathrm{tot}}$, A_p is the area above the p-period orbit partial barrier, and S_{tot} is the total area of the PSOS. We suppose that this inequality is valid for the partial barriers in the deformed cavity as well and apply it as the entering condition.

For the escaping condition, we use the fact that the turnstile area in a PSOS equals the action difference of Birkhoff periodic orbits [24,25]. In our system, the action of a trajectory is its configurational length, due to the uniform refractive index

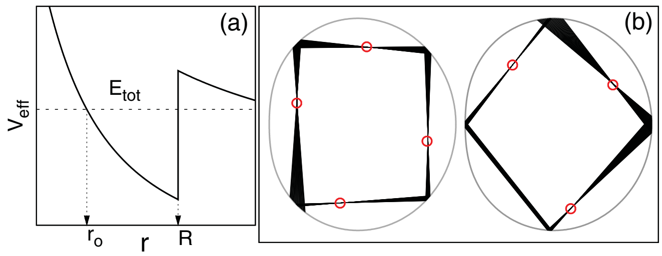

FIG. 5. (Color online) (a) Effective potential along the radial direction in circular microcavities and (b) conjugate points of period-4 orbits for counterclockwise propagation in a Limaçon cavity with $\varepsilon = 0.43$ denoted by open circles (red).

inside. Figure 5(b) shows an example of Birkhoff's pair of the period-4 orbits. From the statement above, the turnstile area in the PSOS is the same as the length difference of the periodic orbits $W_4 = \Delta L_4 = L_\square - L_\diamond$, where $L_\square$ and $L_\diamond$ are the lengths of the square- and diamond-shaped orbits in units of R. In addition, we have to consider a phase sliding, which is given by *conjugate points* [12]. In the semiclassical quantization, each conjugate point is associated with $\pi/2$-phase sliding [26]. The simplest way to assign the conjugate points is the classical ray-tracing calculation with a small bundle of rays around the periodic orbit as the initial condition, which is also confirmed by calculation with the stability matrix. The result of this calculation in our model system reveals an important feature, which is two Birkhoff periodic orbits have a different number of conjugate points, as can be seen in Fig. 5(b). Whereas the square-shaped orbit has four conjugate points on the trajectory, the diamond-shaped orbit has only three points due to the minimum of the boundary curvature. Therefore, the optical length difference of the pair is represented by $\Delta\phi_p = n\,\mathrm{Re}(kR)W_p - \pi\,\Delta m_p/2$, where Δm_p is the difference in the number of conjugate points. The value of Δm_p is given as 1 for all periodic orbits which we consider here. From this phase relation, the escaping condition can be set as the following inequality:

$$\mathrm{Re}(kR) \leqslant \frac{\pi}{2nW_p}. \tag{2}$$

The minimum value of this inequality corresponds to the smallest wave number that can resolve the length difference between a pair of Birkhoff periodic orbits, or the corresponding turnstile area in the PSOS [27]. If a mode does not fulfill this condition, the pair of periodic orbits can play the role of an effective caustic.

The escaping conditions (2), together with the entering conditions (1), are applied and compared to the numerically calculated spectrum. In Fig. 2, the entering condition for a p-period orbit is denoted by black arrows with N_p and the escaping condition by red arrows with E_p. As Fig. 2 shows, the arrows consistently point out the peak range of each convex-curved mode series. Remarkably, the WGMs with the regular feature can be found in a higher spectral region [$n\,\mathrm{Re}(kR) \sim 100$], and the escaping condition works very consistently even there.

From the findings here, the overall mechanism to generate the spectral and modal properties can be concluded as follows: As stated above and shown in Ref. [16], the unidirectional emission results from the chaotic diffusion process following classical unstable manifolds. However, when the action transport through the turnstile is less than the resolution of a wave function, the wave function needs a longer time to resolve the turnstile and the refractive output through the chaotic diffusion is effectively suppressed [28]. Nevertheless, the attenuation of the wave function is still present through evanescent tunneling, limiting the mode lifetime. This limited mode lifetime makes the resolution of the chaotic diffusion even more unlikely. Therefore, the low periodic orbits in the strongly chaotic regime are enabled to confine regular modes, as shown in this Rapid Communication. This can be also understood as an enhancement of the effect of the partial barrier [27] due to the openness. As the refractive output channel through the chaotic diffusion is blocked, the cavity Q factors are increased and the leakage through the tunneling forms bidirectional emission which is tangentially radiated on the cavity boundary, as also shown in Ref. [29].

Based on the quantitative and qualitative understanding presented in this Rapid Communication, the emission directionality and the quality factor of the nanoscaled deformed cavity can be optimized and controlled, especially by choosing the overlap of the gain profile with the spectrum. We expect the finding to improve the controllability of deformed microcavities. Also, the mechanism of the partial barriers confining a mode in a chaotic phase space can be generalized to other kinds of open chaotic systems. Therefore, the findings here can be applied to other quantum systems with irregular properties which we encounter in mesoscopic and nanoscaled systems.

This work is supported by the DFG Research Unit 760.

[1] *Optical Microcavities*, edited by K. Vahala (World Scientific, Singapore, 2005).

[2] D. K. Armani, T. J. Kippenberg, S. M. Spillane, and K. J. Vahala, Nature (London) **421**, 925 (2003).

[3] T. J. Kippenberg, H. Rokhsari, T. Carmon, A. Scherer, and K. J. Vahala, Phys. Rev. Lett. **95**, 033901 (2005).

[4] B. Dayan, A. S. Parkins, T. Aoki, E. P. Ostby, K. J. Vahala, and H. J. Kimble, Science **319**, 1062 (2008).

[5] J. U. Nöckel and A. D. Stone, Nature (London) **385**, 45 (1997).

[6] C. Gmachl, F. Capasso, E. E. Narimanov, J. U. Nöckel, A. D. Stone, J. Faist, D. L. Sivco, and A. Y. Cho, Science **280**, 1556 (1998).

[7] S. Shinohara, M. Hentschel, J. Wiersig, T. Sasaki, and T. Harayama, Phys. Rev. A **80**, 031801(R) (2009); C. Yan, Q. Wang, L. Diehl, M. Hentschel, J. Wiersig, N. Yu, C. Pflügl, F. Capasso, M. A. Belkin, T. Edamura, M. Yamanishi, and H. Kan, Appl. Phys. Lett. **94**, 251101 (2009); C.-H. Yi, M.-W. Kim, and C.-M Kim, *ibid.* **95**, 141107 (2009).

[8] Q. H. Song, W. Fang, B. Liu, S.-T. Ho, G. S. Solomon, and H. Cao, Phys. Rev. A **80**, 041807(R) (2009).

[9] Q. H. Song, L. Ge, A. D. Stone, H. Cao, J. Wiersig, J.-B. Shim, J. Unterhinninghofen, W. Fang, and G. S. Solomon, Phys. Rev. Lett. **105**, 103902 (2010).

[10] M. P. Nezhad, A. Simic, O. Bondarenko, B. Slutsky, A. Mizrahi, L. Feng, V. Lomakin, and Y. Fainman, Nat. Photon. **4**, 395 (2010); J. Shainline, S. Elston, Z. Liu, G. Fernandes, R. Zia, and J. Xu, Opt. Express **17**, 23323 (2010); Z. Liu, J. Shainline, G. Fernandes, J. Xu, J. Chen, and C. Gmachl, *ibid.* **18**, 19242 (2010).

[11] H.-J. Stöckmann, *Quantum Chaos: An Introduction* (Cambridge University Press, Cambridge, UK, 1999).

[12] M. C. Gutzwiller, *Chaos in Classical and Quantum Mechanics* (Springer, New York, 1990).

[13] M. Hentschel and K. Richter, Phys. Rev. E **66**, 056207 (2002).

[14] C. Michel, V. Doya, O. Legrand, and F. Mortessagne, Phys. Rev. Lett. **99**, 224101 (2007).

[15] H. G. L. Schwefel, N. B. Rex, H. E. Tureci, R. K. Chang, A. D. Stone, T. Ben-Messaoud, and J. Zyss, J. Opt. Soc. Am. B **21**, 923 (2004); S.-Y. Lee, S. Y. Lee, J. W. Ryu, T. Y. Kwon, S. Rim, and C. M. Kim, Phys. Rev. A **72**, 061801(R) (2005); S.-B. Lee, J. Yang, S. Moon, J.-H. Lee, K. An, J.-B. Shim, H.-W. Lee, and S. W. Kim, *ibid.* **75**, 011802(R) (2007).

[16] J. Wiersig and M. Hentschel, Phys. Rev. Lett. **100**, 033901 (2008).

[17] J.-B. Shim, S.-B. Lee, S. W. Kim, S.-Y. Lee, J. Yang, S. Moon, J.-H. Lee, and K. An, Phys. Rev. Lett. **100**, 174102 (2008).

[18] A. A. Zembekov, F. Borondo, and R. M. Benito, J. Chem. Phys. **107**, 7934 (1997).

[19] V. A. Podolsky, E. Narimanov, W. Fang, and H. Cao, Proc. Natl. Acad. Sci. (USA) **101**, 10498 (2004).

[20] J. Wiersig, J. Opt. A **5**, 53 (2003).

[21] G. D. Birkhoff, Acta Math. **50**, 359 (1927).

[22] M. Hentschel, H. Schomerus, and R. Schubert, Europhys. Lett. **62**, 636 (2003).

[23] The $\odot$-fixed points correspond to the minimax orbit in the action minimization and the less effective potential is assigned to these points in comparison with the minimizing orbit $\times$. More details can be found in Ref. [24].

[24] J. D. Meiss, Rev. Mod. Phys. **64**, 795 (1992).

[25] R. S. MacKay, J. D. Meiss, and I. C. Percival, Physica D **13**, 55 (1984).

[26] S. C. Creagh, J. M. Robbins, and R. G. Littlejohn, Phys. Rev. A **42**, 1907 (1990).

[27] D. A. Wisniacki, E. Vergini, R. M. Benito, and F. Borondo, Phys. Rev. Lett. **94**, 054101 (2005).

[28] O. Bohigas, S. Tomsovic, and D. Ullmo, Phys. Rep. **223**, 43 (1993); S. Tomsovic and J. H. Lefebvre, Phys. Rev. Lett. **79**, 3629 (1997).

[29] S. C. Creagh, Phys. Rev. Lett. **98**, 153901 (2007).